

## MULTIWAVELENGTH OBSERVATIONS OF EXO 0748–676 – I. REPROCESSING OF X-RAY BURSTS

R. I. HYNES<sup>1</sup>, KEITH HORNE<sup>2</sup>, K. O'BRIEN<sup>3</sup>, C. A. HASWELL<sup>4</sup>, E. L. ROBINSON<sup>5</sup>, A. R. KING<sup>6</sup>, P. A. CHARLES<sup>7,8</sup>, K. J. PEARSON<sup>1</sup>*Accepted for publication in the Astrophysical Journal*

## ABSTRACT

We present the first high time-resolution simultaneous X-ray, ultraviolet, and optical observations of X-ray bursts in UY Vol, the optical counterpart of the low mass X-ray binary EXO 0748–676, obtained with *RXTE*, *HST*, and Gemini-S. Strong reprocessed signals are present in the ultraviolet (a factor of 4) and optical (a factor of 2.5). These signals are lagged with respect to the X-rays and appear significantly smeared as well. The addition of far-ultraviolet coverage for one burst, together with the high quality of the dataset, allow much tighter constraints upon the temperature and geometry of the reprocessing region than previously possible. A single-zone black body reprocessing model for this burst suggests a rise in temperatures during the burst from 18 000 to 35 000 K and an emitting area comparable to that expected for the disk and/or irradiated companion star. The lags, a mean of 4.0 s and range of 2.5 s, are consistent with those expected within the binary. The single-zone black body model cannot reproduce the ratio of optical to ultraviolet flux during the burst, however. The discrepancy, corresponding to underpredicting the optical by more than a factor of two, seems too large to explain with deviations from a local black body spectrum and more likely indicates that a range of reprocessing temperatures are required, as would be expected, with cooler regions not contributing to the UV. Comparable results are derived from other bursts, and in particular the lag and smearing both appear shorter when the companion star is on the near side of the disk as predicted. The burst observed by *HST* also yielded a spectrum of the reprocessed light. It is dominated by continuum, with a spectral shape consistent with the temperatures derived from lightcurve modeling. Some line enhancements are also seen, most prominently in C III 1175 Å. Taken as a whole, our observations confirm the standard paradigm of prompt reprocessing distributed across the disk and companion star, with the response dominated by a thermalized continuum rather than by emission lines.

*Subject headings:* accretion, accretion disks—binaries: close – stars: individual: UY Vol

## 1. INTRODUCTION

The low-mass X-ray binary (LMXB) EXO 0748–676 was discovered in 1985 as a transient X-ray source (Parmar et al. 1985) and rapidly associated with an optical counterpart, UY Vol (Wade et al. 1985). Unlike most X-ray transients, however, it did not decay back to a quiescent state, but remained active and is now considered part of the persistent LMXB population. This makes it an intriguing object for study as it appears to exist near the edge of stability, flipping between phases of quasi-stable activity and quiescence. The likely key to its behavior is that the system is currently held in a meta-stable high state by i) stabilization of the accretion disk against thermal instability by X-ray irradiation and ii) enhancement of the mass transfer rate from the com-

panion. UY Vol is thus an important object for understanding the impact of X-ray irradiation upon the disk and companion star in LMXBs.

UY Vol also has an inclination that is just right to give us a range of diagnostic tools to probe the accretion flow. The inclination is high enough that X-ray eclipses are seen recurring on a 3.82 hr period, and X-ray dips also occur (Parmar et al. 1986). The eclipses are sharp, indicating that the neutron star itself is being eclipsed, and hence that it is visible outside of eclipse. UY Vol is therefore not an accretion disk corona (ADC) source; an ADC is likely present, but is not the dominant source of observed X-rays.

To better understand the accretion structure and effect of irradiation in this LMXB, we have performed a multi-wavelength study using *HST* for UV rapid spectroscopy, *RXTE* for X-ray data, Gemini-S for rapid optical photometry, and the Cerro Tololo 4 m Blanco telescope for optical spectroscopy. We discuss here the analysis of several X-ray bursts seen during the simultaneous coverage. Subsequent papers will address the UV and optical emission line spectra (Pearson et al. 2006, hereafter Paper II), and the spectral energy distribution, and multiwavelength orbital light curves (Paper III).

Type I X-ray bursts, seen in low-mass X-ray binaries (LMXBs) with neutron star primaries, are due to explosive thermonuclear burning of accreted material on the surface of the neutron star. They involve a large increase in the X-ray flux, by a factor of ten or more, on timescales of a few seconds. As well as providing insights into the

<sup>1</sup> Department of Physics and Astronomy, Louisiana State University, Baton Rouge, Louisiana 70803, USA; rih@phys.lsu.edu

<sup>2</sup> School of Physics and Astronomy, The University of St Andrews, St Andrews, KY16 9SS, UK

<sup>3</sup> European Southern Observatory, Casilla 19001, Santiago 19, Chile

<sup>4</sup> Department of Physics and Astronomy, The Open University, Walton Hall, Milton Keynes, MK7 6AA, UK

<sup>5</sup> Astronomy Department and McDonald Observatory, The University of Texas at Austin, 1 University Station C1400, Austin, Texas 78712, USA

<sup>6</sup> Department of Physics and Astronomy, The University of Leicester, University Road, Leicester, LE1 7RH, UK

<sup>7</sup> Department of Physics and Astronomy, The University of Southampton, Southampton, SO17 1BJ, UK

<sup>8</sup> South African Astronomical Observatory P.O. Box 9, Observatory, 7935, South Africa

TABLE 1  
LOG OF UV, OPTICAL, AND X-RAY HIGH TIME RESOLUTION  
OBSERVATIONS.

Facility	Instrumentation	Start date	UT range	Total time (s)
<i>HST</i>	STIS, G140L	2003 Feb 18–19	20:06–00:06	13470
<i>HST</i>	STIS, G230L	2003 Feb 19	00:17–00:31	800
<i>HST</i>	STIS, G140L	2003 Feb 19	00:53–04:52	13470
<i>HST</i>	STIS, G230L	2003 Feb 19	05:04–05:17	800
Gemini-S	AcqCam, <i>V</i>	2003 Feb 18	04:19–05:32	9600
Gemini-S	AcqCam, <i>V</i>	2003 Feb 19	01:08–08:38	18960
<i>RXTE</i>	PCA	2003 Feb 14	00:08–09:32	10300
<i>RXTE</i>	PCA	2003 Feb 15	01:27–09:12	8238
<i>RXTE</i>	PCA	2003 Feb 17	17:21–18:23	3520
<i>RXTE</i>	PCA	2003 Feb 17–18	20:30–08:13	11751
<i>RXTE</i>	PCA	2003 Feb 18	12:17–13:19	1792
<i>RXTE</i>	PCA	2003 Feb 18–19	20:11–09:23	13706
<i>RXTE</i>	PCA	2003 Feb 19	15:07–16:09	3616

conditions on the surface of the neutron star, the sudden flash lights up the whole binary system, and significant reprocessed bursts, with an amplitude of a factor of a few, are seen in the optical (see Hynes 2005 and references therein). Since the reprocessed bursts are a large amplitude signal rather than a small perturbation, the non-linearity of the optical response (due to observing band-limited rather than bolometric fluxes) is clear. Thus lightcurves in different bandpasses exhibit significant differences, breaking the degeneracy between the temperature and emitting area of the reprocessing region that exists when only small perturbations are considered (Lawrence et al. 1983). This makes the bursts a very powerful tool for applying echo mapping techniques in an X-ray binary (e.g. O’Brien et al. 2002; Hynes 2005).

In spite of this potential, the unpredictable nature of the bursts means that relatively few simultaneous observations exist of any X-ray bursting source, many twenty years old, and no UV observations of bursts have been obtained. We present here the first simultaneous X-ray, UV, and optical observations of a burst in UY Vol, including fast far-UV spectroscopy. We also present several more bursts observed with only X-ray and optical coverage.

## 2. OBSERVATIONS

### 2.1. *HST*

*HST* observations used the Space Telescope Imaging Spectrograph (STIS; Profitt et al. 2002), with the far-UV MAMA detector and the G140L grating, and are detailed in Table 1. TIMETAG mode yielded a stream of detected events, with 125  $\mu$ s precision, which could be used to reconstruct spectra for any desired time-interval, as well as high time-resolution lightcurves. The observations were timed such that the target was within the continuous viewing zone (CVZ). Consequently we were able to observe over about 9 hrs with only small gaps for wavelength calibrations and mode changes. This covered two complete binary orbits.

To obtain a lightcurve, we extracted source counts from a 50 pixel wide window centered on the target and background from two similar regions on either side. Geo-

coronal H I Ly $\alpha$  and O I 1304  $\text{\AA}$  lines were masked out of both source and background regions, as were the extreme ends of the detector. It was necessary to use this background subtraction procedure as the background was found to be larger than the nominal global 7 cnt  $\text{s}^{-1}$  dark current and time dependent. This intermittent ‘glow’ is not easily modeled (Profitt et al. 2002) so is best removed empirically. We did this by subtracting a polynomial fit to the background lightcurve. Source counts out of burst were  $\sim 30 – 100 \text{ s}^{-1}$  and the estimated background within the source window was  $\lesssim 7 \text{ s}^{-1}$ ; for comparison the nominal dark current should only be  $\sim 0.3 \text{ s}^{-1}$  within this window.

We used 1 s time-resolution to approximately match the Gemini-S optical photometry. As discussed by Hynes et al. (2003), *HST*/STIS absolute timing accuracy is uncertain at a level of up to a few seconds, so we did not attempt precise barycenter corrections and allowed the zero point of the *HST* timing to be a free parameter in subsequent analysis.

Flux calibration of the lightcurves was derived from the average spectra, and takes advantage of the reddening measurement ( $E(B - V) = 0.06 \pm 0.03^9$ ) possible with complementary near-UV data (see Paper III). For each G140L spectrum we compared the observed counts as a function of wavelength with the dereddened fluxes (Fitzpatrick 1999) to determine the effective sensitivity, hence defining our far-UV bandpass. We then used this sensitivity function to derive weighted average wavelengths and fluxes. These averages were consistent to  $\lesssim 1 \text{ \AA}$  in wavelength, and  $\lesssim 1\%$  in flux between the six G140L spectra. The effective wavelength derived (for our spectral shape) was 1388  $\text{\AA}$ . The uncertainty in the calibration of observed fluxes is 4% (from the documented flux calibration of low-resolution STIS/MAMA modes; Profitt et al. 2002). However, the dominant term is due to the uncertainty in dereddening – this introduces a  $\pm 25$  percent uncertainty in the absolute calibration of the far-UV lightcurves, and  $\pm 16$  percent in the relative calibration of the UV and optical fluxes (since these errors are correlated). If the extinction curve differs from the assumed Fitzpatrick (1999) form then the error could be larger.

### 2.2. *Gemini-S*

On the nights of February 17–18 and 18–19, we used the Acquisition Camera (AcqCam) on Gemini-South to obtain fast *V* band optical photometry (see Table 1 for details). Conditions were photometric, with realized image quality on target mostly  $\sim 0.9 \text{ arcsec}$ , although this degraded to  $\sim 1.2 \text{ arcsec}$  in the latter part of the second night. For practical data acquisition it was necessary to break each night into series of (usually) 4000 images at a time. The series obtained, totaling 37 000 images, are listed in Table 1.

One of the great strengths of this instrument for fast photometry is the fast readout. We used the camera windowed and binned ( $2 \times 2$  giving  $256 \times 256 0.24 \text{ arcsec}$

<sup>9</sup> Note that this is substantially below the previously quoted value of 0.4 (Schoembs & Zoeschinger 1990; Liu et al. 2001). Since that value was based on shifting the object to lie on the main-sequence in a color-color diagram, it is not expected to be reliable for an LMXB

binned pixels). Other data acquisition modifications were made to further minimize the dead-time between images. This dead-time was not absolutely constant, but was usually 0.305–0.310 s, with occasional (less than one per few hundred) glitches to as high as 0.44 s. The precise time-stamps were taken from when the image completed writing to disk, so the start time of the subsequent image (relative to the first in a series) was known. The start time of the first image is taken from a GPS based clock.

Basic reductions including bias removal, subtraction of the significant dark current, and flat-fielding were done using the AGREDUCE script within IRAF<sup>10</sup>. The windowed field includes one star much brighter than UY Vol, which provided a high fidelity reference star and two other comparisons (one brighter, one fainter) which were used to verify the accuracy of the results. We experimented with both small aperture photometry using IRAF and optimal photometry as implemented in the Starlink PHOTOM package (see Naylor 1998 for the algorithm this is based on). We found negligible difference between the two methods provided the aperture (for unweighted photometry) was optimized. We opted to use the results from the optimal algorithm as this explicitly adjusts the weighting per image and so should be more robust against changes in seeing. We used the comparison stars to verify that the standard deviations of the resulting lightcurves are dominated by the formal errors in the photometry. The formal errors for UY Vol were typically  $\sim 2.5$  percent per 0.8 sec exposure.

Absolute calibration was done with respect to two stars from SA 104 (Landolt 1992) on the first night. We derive magnitudes of  $V = 13.63$  for the reference star and 17.4–18.0 for UY Vol (excluding bursts). The magnitude range derived for UY Vol is within the range observed by earlier studies (e.g. 17.1–18.1; van Paradijs, van der Klis, & Pedersen 1988). The orbital lightcurves will be considered in a subsequent paper.

Finally, we corrected the observed magnitudes for interstellar extinction (assuming  $E(B - V) = 0.06$  based on the 2175 Å feature in our *HST* data) and converted to fluxes with the conversion constant of Fukugita, Shimasaku, & Ichikawa (1995).

### 2.3. RXTE

X-ray observations were obtained with the Rossi X-ray Timing Explorer (*RXTE*) in two blocks timed to coincide with optical spectroscopy (Paper II), and the optical and UV observations described above. A log is presented in Table 1.

X-ray lightcurves of the bursts were recovered from a 64 channel event mode of the Proportional Counter Array (PCA). See Jahoda et al. (2006) for discussion of the current status of the PCA. Since the source counts are high during a burst, and the timescale is short, we used all PCUs which were switched on, including PCU0. We initially processed lightcurves from each PCU separately, however, to check that no background flares were present in PCU0, before combining them. Back-

ground lightcurves (with 16 s time-resolution) were constructed from the L7/240 faint source combined models dated 2002 Feb 1. This should allow the most reliable background subtraction from the pre-and post-burst lightcurves. Since the L7 rate is modified for bright sources, however, this model lightcurve is contaminated during the burst. We therefore interpolated between the pre- and post-burst modeled background rates to define the burst background and subtracted this. We note that in practice the background subtraction has little impact on the results described here as we perform an additional empirical subtraction of the persistent (pre- and post-burst) flux. Hence more refined background models would not significantly affect our results.

Lightcurves were initially extracted for 2–5 keV, 5–12 keV and 12–60 keV bandpasses. The burst profiles varied significantly with energy, so it is important to be careful in choosing an appropriate lightcurve for a deconvolution. We therefore also constructed a 2–20 keV integrated flux lightcurve. To do this, we estimated approximate per-channel conversions from count rates to fluxes using XSPEC and appropriate response matrices. We used a black body fit to the average burst spectrum to define these conversions to ensure that the relative weighting within each channel was approximately correct. We then applied these conversions to each channel and summed the fluxes. This will be somewhat noisier than a straight sum of count rates, but represents our best estimate of the evolution of the flux irradiating the disk and the companion star. Based on the black body fits to the spectra, the 2–20 keV bandpass accounts for most of the burst flux ( $\gtrsim 90\%$ ), so additional bolometric corrections are ignored.

### 3. SYSTEM PARAMETERS

Any attempt to quantitatively model observations of UY Vol requires system parameters. UY Vol does not yet benefit from dynamical estimates, so we must use more indirect constraints.

Fortunately it is eclipsing, and precisely defined X-ray eclipses provide exquisitely detailed measurements of the orbital period and duration of the neutron star eclipse (Wolff et al. 2002). Through these eclipses, we know that the inclination must be high, and the relationship between mass ratio and inclination is well defined. Assuming recent eclipse durations of  $497.5 \pm 6.0$  s, we obtain the relationship shown in Fig. 1. We can attempt to further constrain the available parameter space in other ways. The fact that we see the sharp neutron star eclipse at all indicates that UY Vol is not an accretion disk corona (ADC) source. This means the inclination cannot be too high as our line-of-sight must pass over the disk rim. The disk rim height is not known directly, but must be greater than that expected from hydrostatic support alone. This is a very weak constraint, however; for example, for a disk half-thickness of 0.03, we only require  $i < 88.3^\circ$ . This constraint is shown in Fig. 1.

Other constraints are more model-dependent. We can make plausible estimates of the range of mass ratios likely, although values outside of this range are still possible. The companion star to UY Vol is probably above the hydrogen burning limit and non-degenerate. This implies  $M_2 \gtrsim 0.07 M_\odot$  (Chabrier & Baraffe 2000). Assuming a  $1.35 M_\odot$  neutron star (Thorsett & Chakrabarty

<sup>10</sup> IRAF is distributed by the National Optical Astronomy Observatories, which are operated by the Association of Universities for Research in Astronomy, Inc., under cooperative agreement with the National Science Foundation.

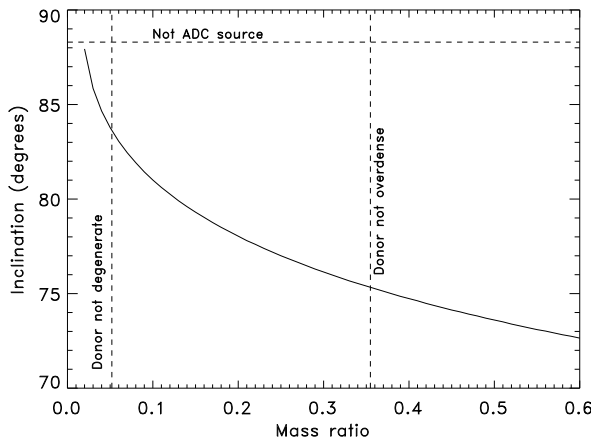


FIG. 1.— Relation between inclination and mass ratio based on the widths of X-ray eclipses.

1999) then yields a minimum mass ratio of 0.05. This limit is soft, as a more massive neutron star is certainly possible if it has accreted significant mass from the companion (as seems likely in 2S 0921–630; Shabbaz et al. 2004; Jonker et al. 2005). At the high mass-ratio end, we can assume that the companion star is underdense compared to a main-sequence star that would fill the Roche lobe. Again assuming a  $1.35 M_{\odot}$  neutron star this yields the upper limit on the mass ratio shown. This could be increased a little for a somewhat lower mass neutron star, and further if the companion is actually overdense. This is possible if the companion had undergone nuclear evolution, before losing most of its envelope in mass transfer (Schenker & King 2002; Haswell et al. 2002). In this case the neutron star might also be expected to be more massive. Consequently, there is probably not much scope for a mass ratio higher than 0.4 in this system.

It should be noted that the constraints considered so far are effectively the same as obtained by Parmar et al. (1986), namely  $75^\circ < i < 82^\circ$ . As discussed above, the limits are rather soft, and a slightly larger range is possible with a companion star and/or neutron star with extreme properties.

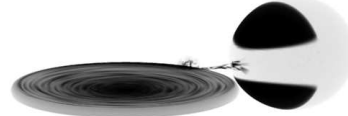
To obtain other parameters of interest, we synthesize a population of possible binaries. We assume the known orbital period, and the relationship between mass ratio and inclination given in Fig. 1. We consider neutron star masses with an asymmetric Gaussian distribution  $M_1 = 1.35^{+0.2}_{-0.04} M_{\odot}$ , i.e., following (Thorsett & Chakrabarty 1999), but allowing for a higher mass tail due to mass transfer. We assume a uniform distribution of companion star masses between  $0.07 M_{\odot}$ , and the mass at which main-sequence density is reached.

We derive a relatively narrow range of binary separations,  $(1.03 \pm 0.05) \times 10^{11} \text{ cm}$  (at 90 % confidence), since the binary period is known and there is not a large uncertainty in the total system mass. Disk parameters are more uncertain; the tidal truncation radius is  $(0.50 \pm 0.05) \times 10^{11} \text{ cm}$  and the projected area of a flat disk would be  $(1.5 \pm 0.2) \times 10^{21} \text{ cm}^2$ . The projected area of the companion star, with a spherical approximation, would be  $(2.0 \pm 0.9) \times 10^{21} \text{ cm}^2$ . While in general,

Model 2:  $q=0.20, i=78$   
MB1: Phase=0.20



Model 2:  $q=0.20, i=78$   
MB2: Phase=0.38



Model 2:  $q=0.20, i=78$   
MB3: Phase=0.48-0.51

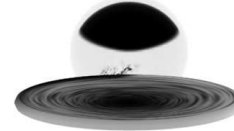


FIG. 2.— System geometry at the phases where bursts were observed for model 2.

the companion is expected to subtend a larger projected area than the disk, only a phase-dependent fraction of this will be X-ray heated, so this should be considered an upper limit on the area of the luminous regions of the companion, which could be significantly less than that of the disk.

We can estimate light travel times in the same way. The maximum lag from the pole of the companion star would be  $(6.8 \pm 0.3) \text{ s}$  at phase 0.5, although most of the heated inner face would of course be a little shorter than this. Lags from the disk would be expected to span a range from zero to  $(3.3 \pm 0.3) \text{ s}$  assuming it extends to the tidal truncation radius.

We define several test cases consistent with Fig. 1: model 1 has  $q = 0.08, i = 82^\circ$ . Model 2 has  $q = 0.2, i = 78^\circ$ , and model 3 has  $q = 0.34, i = 75.5^\circ$ . Fig. 2 shows a schematic view corresponding to model 2 at phases when bursts were observed.

An important factor in considering irradiation of the companion star is the opening angle of the disk,  $\beta$ . For our purposes, this defines the height of X-ray absorbing material, which may be above the optical photosphere, and may not be in hydrostatic equilibrium (for example material thrown up from the stream impact point or local flares). Values derived from other objects have generally been rather high. de Jong, van Paradijs, & Augusteijn (1996) derived  $\beta = 12^\circ$  and cite other authors who obtained a range of  $6\text{--}14^\circ$ . In our case, the highest values are ruled out in some models, as UY Vol is not an

TABLE 2  
BURSTS DETECTED DURING OUR OBSERVATIONS

Burst ID	Wavelengths	UT date and time	Phase
XB1	X-ray	2003 Feb 15, 05:27:06	0.22
XB2	X-ray	2003 Feb 18, 01:15:16	0.95
MB1	X-ray, opt.	2003 Feb 18, 06:01:38	0.20
MB2	X-ray, opt., UV	2003 Feb 19, 01:49:12	0.38
MB3a	X-ray, opt.	2003 Feb 19, 06:01:36	0.48
MB3b	X-ray, opt.	2003 Feb 19, 06:09:08	0.51

ADC source – we see neutron star eclipses and prominent bursts, hence we do observe the neutron star directly. Thus the opening angle must be less than  $90 - i$ , i.e. less than  $12^\circ$  for model 1 and less than  $8^\circ$  for model 2. This is not a constraint for model 3. Note that the presence of eclipses also indicates that at least some of the companion star must be exposed to direct radiation from the neutron star; it cannot be fully shielded by the disk.

A final important parameter is the distance to UY Vol. The best indicator of this is in neutron star LMXBs is the peak flux observed during radius expansion X-ray bursts as this is believed to be an approximate standard candle (Kuulkers et al. 2003). Three radius expansion bursts were reported by Gottwald et al. (1986) and Jonker & Nelemans (2004) used these, together with the calibration of (Kuulkers et al. 2003), to derive a distance range to UY Vol of 6.8–9.1 kpc, with the low end of the range corresponding to burning of material of normal composition and the upper end to hydrogen poor material. More recently, Wolff et al. (2005) used a brighter radius expansion burst seen by *RXTE* to obtain distances of  $5.9 \pm 0.9$  kpc or  $7.7 \pm 0.9$  kpc for hydrogen rich and poor bursts respectively. The latter authors argue that the variation in brightness likely reflects variable obscuration and hence that their brighter burst gives a more reliable distance measurement. We will thus use the midpoint of the latter estimates for this work, 6.8 kpc. Allowing for the composition ambiguity, all luminosities and estimated areas quoted in this work will then be uncertain by  $\pm 50\%$  due to the uncertain distance.

#### 4. BURSTS DETECTED

Our *RXTE* coverage detected a total of 6 bursts, including two weak ones, listed in Table 2. One of these, MB3b, was observed in a pair where the second is weaker than the first, and the other, XB1, could also have been preceded by an unobserved normal burst as it occurs at the beginning of a time-series. Four of these bursts, including the pair, were observed by Gemini-S and one of these also by *HST*, giving X-ray, UV, and optical coverage of the same burst. The data quality in the UV, and especially the optical, is superb, making these the best observed optical bursts in any source. The bursts with multiwavelength coverage are shown in Fig. 3.

One of the simultaneously observed bursts, MB3a, shows dips in the otherwise smooth decay. This burst occurred at orbital phase 0.478, so does not lie within the classical dipping phase-range but our X-ray data do appear to show additional dipping near phase 0.5 (Paper III), so it might be due to transient absorption by

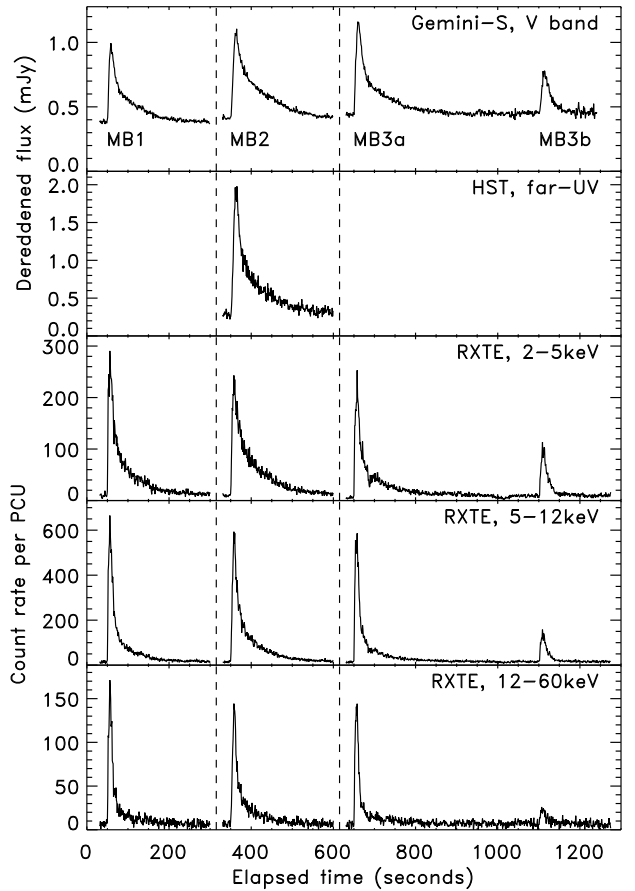


FIG. 3.— X-ray bursts with simultaneous multiwavelength coverage. These have been arbitrarily shifted in time to fit on common axes. Dashed lines indicate non-contiguous coverage.

intervening material. In support of this, the dip does appear most pronounced in the 2–5 keV energy band, and is absent in the optical data. Both these characteristics suggest that the dips are due to absorption of the direct X-rays along our line-of-sight, rather than variations in the intrinsic burst luminosity.

#### 5. BURST ANALYSIS

##### 5.1. Cross-correlation Functions

Cross-correlation functions (CCFs) provide a relatively simple technique for examining lags between lightcurves, and one which is widely used allowing comparison with other datasets. We therefore begin with this approach, before developing other techniques customized to the reprocessed burst problem. The datasets we have are almost exactly evenly sampled, but the Gemini-S photometry has a somewhat longer sampling interval than the *RXTE* or *HST* data. Interpolation cross-correlation functions (Gaskell & Peterson 1987; White & Peterson 1994) are thus ideally suited to these data. We show all of the CCFs in Fig. 4. The single, strongly correlated signal makes identification of the peak very easy, and its location is well defined. A lag of a few seconds is clearly seen, with individual values tabulated in Table 3. All lags are of order a few seconds, as expected for light travel times within the binary. All full strength

TABLE 3  
LAGS MEASURED FROM CCF.

Burst ID	Wavelengths	CCF	Lag	Phase
MB1	X-ray, opt.	2.92	0.20	
MB2	X-ray, opt.	4.14	0.38	
MB2	X-ray, UV	4.01	0.38	
MB3a	X-ray, opt.	4.09	0.48	
MB3b	X-ray, opt.	4.30	0.51	

bursts show rather similar structure, and asymmetry between the rising and decaying portions. For MB3a and MB3b, the lags derived are consistent, but the shapes of the CCF are not. The CCF lags do suggest a positive correlation between orbital phase and mean lag, but the evidence is not compelling (and would vanish if MB1 were removed from the sample). Nonetheless, this is as expected if there is a significant contribution to the reprocessed signal from the surface of the companion star, as the lag from this will be minimum at phase 0.0 and maximum at phase 0.5. This behavior is also consistent with the finding of Schoembs & Zeschinger (1990) that the *rise time* of optical bursts (without simultaneous X-ray coverage) was correlated with the orbital phase in the same sense.

Obviously before extensive interpretation, more sophisticated analysis is warranted to verify these results. The quality of the CCFs are superb and the major concern relates to the meaningfulness of the lag derived. Fundamental to the CCF approach is the assumption that the optical/UV is simply a lagged version of the X-rays, but this is clearly not the case in the burst lightcurves, and is not expected theoretically. Several factors may be important. One is light travel times. These will not only produce a mean lag, but will tend to smear out the signal, as different lags are produced by different reprocessing sites (O'Brien et al. 2002). A second factor having a similar effect is that there may be a finite diffusion time associated with reprocessing; if X-rays deposit energy at a significant optical depth it cannot be re-radiated instantly, but there will be further lagging and smearing as the energy diffuses outward. Finally, the tails of the bursts are clearly different, indicating non-linear relationships between the lightcurves. This occurs because the bursts have a large amplitude and substantially change the temperature of both the neutron star and the reprocessing site. As a site cools, the peak of the emitted spectrum moves to lower energies. In the case of the reprocessed light, it moves out of the far-UV, and into the optical, having the effect of accelerating the far-UV decay rate (relative to the bolometric decay) and suppressing the optical decay. None of these factors are accounted for in cross-correlations, so a more sophisticated model is needed. For example, lags can be over or under-estimated if the timing characteristics of the two lightcurves differ (Koen 2003), reflecting the more general problem that in this case there is not a uniquely defined lag. There is a range, from which a CCF favors an average value.

## 5.2. Maximum Entropy Deconvolutions

We next attempt to deconvolve the lightcurves to obtain the transfer function between X-ray and optical wavelengths independent of the width of the burst. This will be more readily interpreted than the CCF which is much broader than the transfer function. We initially use the maximum entropy method (MEM; Horne et al. 1991; Horne 1994), which does not require an assumed model for the transfer function, beyond an assumed default used in calculating entropy. In principle, the MEM method can then resolve distinct sub-structures, if they are present, for example the disk and companion star.

For each burst we use our X-ray flux lightcurves as the driver signal and attempt to fit the optical or UV echo over the range  $-50$  to  $+300$  s relative to the burst rise. The transfer function was calculated for lags of  $-50$  s to  $+200$  s. We use a narrow Gaussian default to minimize enforced smoothing of the derived transfer functions. The results are shown in Fig. 5. Negligible response was seen before  $-10$  s, and slow declines after  $+50$  s; these regions are not shown.

As expected, the derived transfer functions are much narrower than the CCFs. All bursts suggest a single-peaked response peaking at a lag of a few seconds, very close to the locations of the maxima of the corresponding CCFs. Besides the main peak, all the transfer functions have a tail extending to larger lags. This may be a real effect, as models of reprocessing of bursts by stellar atmospheres do predict a small amount of the energy emerges with large delays (Cominsky, London, & Klein 1987; see Section 7.2 for more discussion). We cannot say with confidence that this effect is real, however, as there is another explanation for it. As noted earlier, the bandpass-limited response is non-linear, and in particular the optical burst decay is much slower than that in X-rays because the reprocessed spectrum shifts to longer wavelengths (into the optical band) as it cools. A method which assumes a linear response will require an extended tail to reproduce this. In support of this interpretation, the effect is much weaker in the transfer function derived from UV data as expected.

This effect complicates the interpretation of the shape of the transfer functions using this method. In addition, while it is tempting to ascribe the narrower transfer function from MB1 to a phase-dependent effect, the response to MB3a is also narrower, and in general one has to be cautious in interpreting widths derived from MEM echo maps as a broader, smoother peak inherently has higher entropy. We therefore seek a less biased approach.

## 5.3. Gaussian Transfer Function Fitting

### 5.3.1. Method

Hynes et al. (1998) demonstrated a method for constraining the transfer function by parameterizing it as a Gaussian function. Our MEM reconstructions indicate that the data do not require multiple resolved components in the transfer function. This does not mean that the true transfer function does not include multiple components; only that they are not well constrained by the data. This is probably a consequence of the relatively long burst timescale, which limits our sensitivity to fine temporal structure in the response. Consequently the single Gaussian transfer function is an adequate approximation to this problem and it lends itself well to adapt-

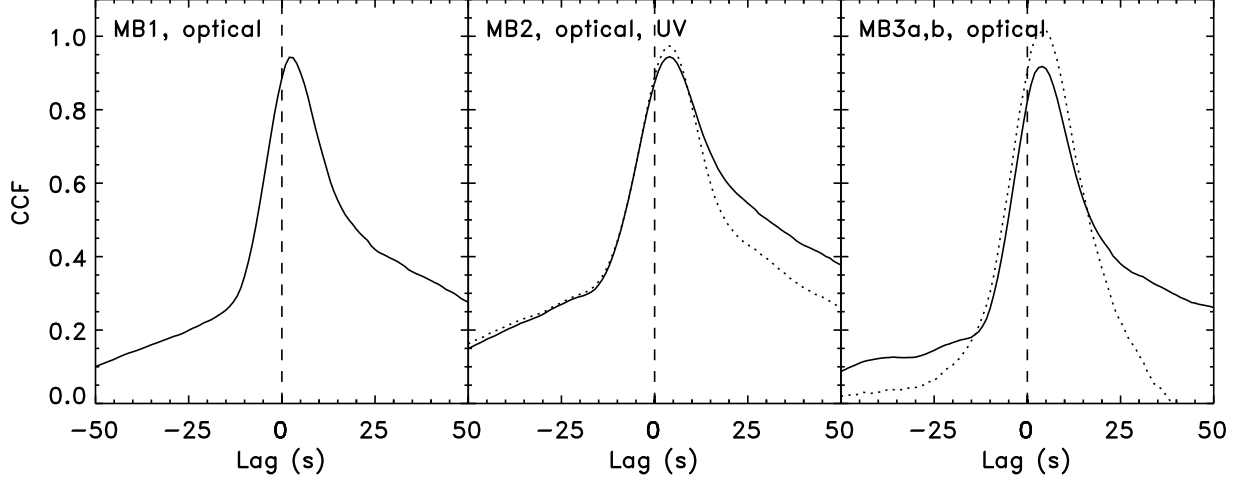


FIG. 4.— Cross-correlation functions for the bursts. The optical or UV broad-band data are cross-correlated against the integrated X-ray flux lightcurves. For MB2, the solid line shows the result with optical data, the dotted one that with UV. For MB3, the solid lines shows MB3a, the dotted one MB3b.

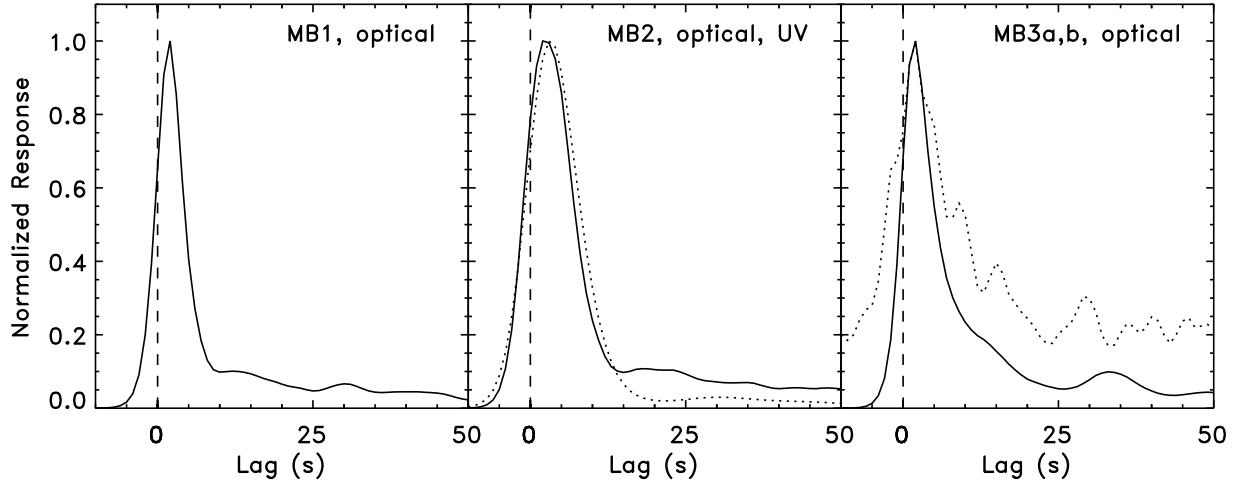


FIG. 5.— MEM reconstructed transfer functions for the simultaneous bursts. For MB2, the solid line shows the result with optical data, the dotted one that with UV. For MB3, the solid lines shows MB3a, the dotted one MB3b.

ing to the rather different assumptions needed for burst mapping.

These arise because of the large amplitude of the variations. We have already discussed one problem this causes; the X-ray lightcurves are strongly energy dependent, so determining the driving lightcurve is non-trivial. This arises because the X-ray flux arises from heating and cooling of the neutron star surface; as the surface cools, the spectrum softens and moves out of the higher energy bands. We have addressed this by calculating a 2–20 keV integrated flux lightcurve, using the spectral information to ensure the correct internal relative weighting. Similar difficulties exist with the optical and UV data. The optical burst is more prolonged than the UV one, for the same reason as the bursts are more prolonged at low energies; the reprocessed spectrum is moving out of the UV band into the optical as the reprocessing regions cool. The net

effect of this is that the optical and UV fluxes do not respond linearly to the X-ray flux, and the amplitude of the variations is too large for them to be treated as a small, linearized perturbation. This is actually a blessing in disguise however, as we can then use the relative changes between the optical and UV fluxes to constrain the temperature evolution, and hence also the emitting area of the reprocessing region. Without this information, there would be a degeneracy between temperature and area, and indeed this is a problem when we try to fit optical or UV data independently. For example, Lawrence et al. (1983) attempted a similar analysis of 4U 1636–536 using *UBV* photometry and were able to estimate that the bursts involved a rise in temperature of the reprocessor from  $\sim 25,000$  K to  $\sim 50,000$  K.

We formulate the problem as follows. We assume that an input X-ray lightcurve (the 2–20 keV integrated flux)

is a suitable proxy for the bolometric illuminating luminosity,  $L_X$ . Reprocessing is assumed to occur within a fixed area  $A$  (assumed to be of negligible geometric depth) with uniform temperature  $T(t)$ . The spatial position and extent of this region introduces a mean lag,  $\tau$ , and a blur  $\sigma_\tau$  in the reprocessed bolometric luminosity relative to the illuminating luminosity. The temperature is then allowed to vary (with fixed reprocessing area) such that  $T^4(t) \propto L_{\text{rep}}$ , where the reprocessed luminosity is assumed to be related to the X-ray luminosity via the transfer function,  $\Psi$ :  $L_{\text{rep}} \propto \Psi * L_X$ . Given the temperature evolution and area we can then predict the bandpass-limited UV and optical flux evolution. This requires a model for the reprocessed spectrum, for which we assume a black body in the absence of a better choice. The problem can be parameterized in terms of  $\tau$  and  $\sigma_\tau$ , defining the transfer function (which is arbitrarily normalized),  $T_{\text{min}}$  and  $T_{\text{irr}}$  which are the minimum temperature and the peak irradiation temperature, defined such that  $T_{\text{max}}^4 = T_{\text{min}}^4 + T_{\text{irr}}^4$ , and  $A$ , the projected cross-sectional area of the reprocessing region. Ideally this gives enough parameters to fit the UV and optical lightcurves simultaneously. In practice, some additional nuisance parameters are needed. Since the *HST* absolute timing is uncertain, we fit the optical and UV lags independently; the optical should be reliable, but the UV one is not, comprising both a true lag and a clock uncertainty. We also allow the optical and UV bursts to have different reprocessing areas. This is initially assumed to reflect uncertainties in the calibration of the optical photometry and in dereddening of the optical:UV flux ratio, rather than physical differences. In the ideal case, both lags and both areas would be equal.

### 5.3.2. The multiwavelength burst (MB2)

We begin with the burst which has both UV and optical coverage as this should be best constrained. It also allows us to test the reliability of the optical fit by comparing it with the joint optical-UV fit.

We search for the best fitting models (in the  $\chi^2$  sense) using a downhill simplex method (Press et al. 1992). To guard against converging on a local minimum each fit used three passes, each starting at the previous best fit, and we also varied the initial starting simplex to approach the minimum from different directions in parameter space. We find that the method can reproduce both the optical and UV lightcurves very well. The best fitting joint model (MB2-1) is shown in Fig. 6 and Table 4, with approximately the same parameters found for a variety of starting simplexes. There was a small jitter dependent on the starting point, but this was much less than the uncertainties that we estimate, so all fits agreed to within errors. The best fitting reduced  $\chi^2$  is 1.85, but this is pessimistic. The reason is that we have used the X-ray lightcurve to construct the model, and its errors have not been accounted for. To compensate for this in deriving estimates of errors on the fit parameters, we use the common technique of rescaling the errors so that the best fit model has  $\chi^2/\text{dof} = 1$ .

The model derived has reasonable parameters. The heated region has a quiescent temperature of 18,500 K and is heated to a peak temperature of 36,000 K. The mean lag is 4.0 s, and there is considerable smearing, with a FWHM of 5.8 s. The implied error in the *HST* timing

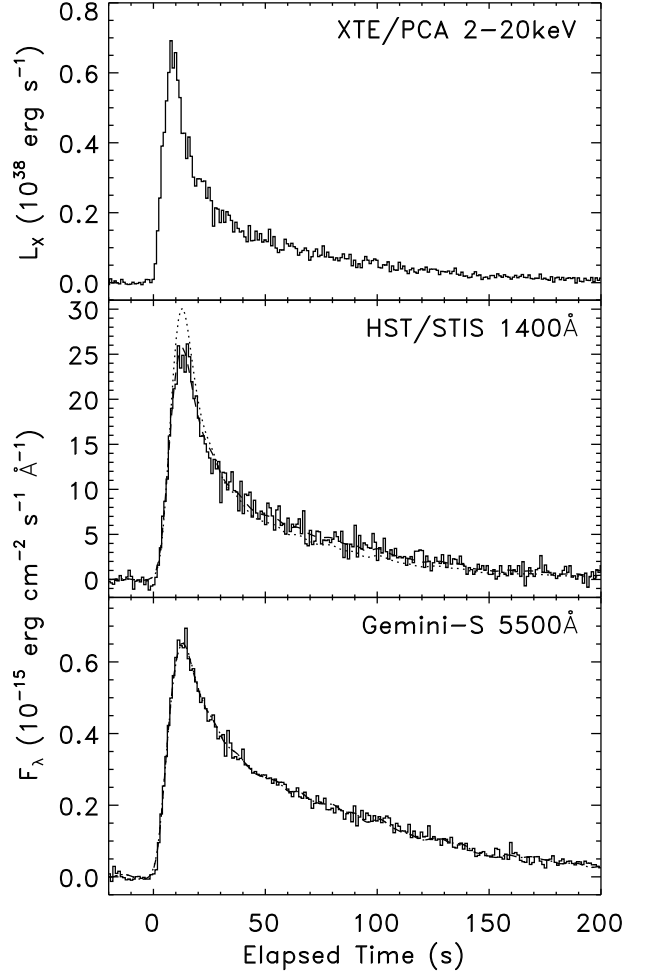


FIG. 6.— Single black body fits to MB2, allowing the optical-to-UV areas to float independently (dashed line), or fixing them to the same value (dotted line). The underlying non-burst X-ray luminosity that has been subtracted off is  $2.1 \times 10^{36} \text{ erg s}^{-1}$ .

is only 0.2 s, which is better than might be expected. The lag is of the order expected for a combination of disk and companion star reprocessing, but the smearing involved is large. The inferred emitting projected area is  $0.9 \times 10^{21} \text{ cm}^2$  from the UV data and  $1.9 \times 10^{21} \text{ cm}^2$  using the optical. The areas derived are fully consistent with expectations from reprocessing on the accretion disk ( $1.5 \pm 0.2 \times 10^{21} \text{ cm}^2$ ) and/or companion star ( $2.0 \pm 0.9 \times 10^{21} \text{ cm}^2$ ). The large discrepancy in the area derived from the optical and UV is more problematic, however, indicating that the optical/UV flux ratio is very different from that implied by the temperatures; the optical is a factor of  $\sim 2$  brighter than expected. This is much larger than can be accommodated from errors in the dereddening (16%), UV flux calibration (4%) or optical calibration (probably less than 10%). The difference is clearly significant; a similar fit with the areas forced to be equal (MB2-2) results in a visibly poor fit to the UV lightcurve. Since the derived magnitudes are already at the low end of the range observed by previous studies it is more likely that the optical flux has been

TABLE 4  
FITS TO BURSTS WITH GAUSSIAN TRANSFER FUNCTIONS.

Burst model	$\tau_{\text{opt}}$ (s)	$\tau_{\text{uv}}$ (s)	$\sigma_{\tau}$ (s)	$T_{\text{min}}$ (K)	$T_{\text{irr}}$ (K)	$A_{\text{opt}}^{\text{a}}$ (cm $^2$ )	$A_{\text{uv}}^{\text{a}}$ (cm $^2$ )	$\chi^2/\text{dof}$
MB1-1	$2.57 \pm 0.02$	–	$0.43 \pm 0.01$	[18500]	$34800 \pm 500$	$(1.88 \pm 0.03) \times 10^{21}$	–	1.19
MB1-2	$2.44 \pm 0.04$	–	$1.23^{+0.06}_{-0.11}$	[18500]	$35400 \pm 400$	$(1.72 \pm 0.02) \times 10^{21}$	–	1.33
MB2-1	$4.05 \pm 0.07$	$3.80 \pm 0.18$	$2.48 \pm 0.08$	$18500 \pm 700$	$35300 \pm 1200$	$(1.92^{+0.09}_{-0.07}) \times 10^{21}$	$(0.87^{+0.12}_{-0.09}) \times 10^{21}$	1.85
MB2-2	$4.12 \pm 0.08$	$3.81 \pm 0.16$	$2.62 \pm 0.09$	$13600 \pm 100^{\text{b}}$	$26700 \pm 200^{\text{b}}$	$(2.65 \pm 0.05) \times 10^{21}$	–	2.12
MB2-3	$4.05 \pm 0.07$	$3.80 \pm 0.17$	$2.48 \pm 0.08$	$12000 \pm 700$	$23500 \pm 1200$	$(2.32 \pm 0.01) \times 10^{21}$	$(1.31^{+0.09}_{-0.05}) \times 10^{21}$	1.85
MB2-4	$4.08 \pm 0.07$	$3.81 \pm 0.16$	$2.54 \pm 0.09$	$9100 \pm 100^{\text{b}}$	$18700 \pm 100^{\text{b}}$	$(3.03 \pm 0.02) \times 10^{21}$	$(3.03 \pm 0.02) \times 10^{21}$	1.90
MB2-5	–	$3.78 \pm 0.15$	$2.43 \pm 0.21$	[18500]	$35900 \pm 1500$	–	$(0.82^{+0.12}_{-0.09}) \times 10^{21}$	1.11
MB2-6	$4.05 \pm 0.08$	–	$2.48 \pm 0.10$	[18500]	$35300 \pm 400$	$(1.92 \pm 0.05) \times 10^{21}$	–	2.69
MB3-1	$4.02 \pm 0.09$	–	$2.69 \pm 0.11$	[18500]	$32700 \pm 500$	$(2.50^{+0.03}_{-0.04}) \times 10^{21}$	–	4.57

<sup>a</sup>The errors quoted on areas only include statistical uncertainties; distance, reddening, and calibration uncertainties will dominate.

<sup>b</sup>These uncertainties are unrealistically small. In this model, the temperature is set precisely by the ratio of optical to UV flux, but the uncertainty only includes statistical errors.

underestimated than that it has been overestimated by a magnitude as required. If the extinction curve is far from the Galactic average, then a larger reddening correction to the UV is possible, and this could rectify the problem.

Alternatively, there may be a deficiency in the model. The most likely interpretation is that the reprocessing region is not isothermal; indeed this is not expected to be the case. The disk is expected to span wide range of temperatures from rim to center, and the companion star will provide an additional reprocessing site. A multi-temperature spectrum will be broader than a single temperature one, and if the peak is in the UV (as implied by the derived temperatures), then this will flatten the optical tail and increase the optical fluxes. A simple test of whether this explanation can help resolve the discrepancy is to use simple irradiated disk spectra as discussed by (Hynes et al. 2002). Instead of using black bodies of temperature  $T$ , we use irradiated disk spectra with irradiation temperature at the edge  $T$ , and viscous temperature set to zero. In practice the latter constraint only means that the temperature is dominated by irradiative heating; increasing the viscous temperature reduced the quality of the fit. Models MB2-3 and MB2-4 show parameters derived using this alternate spectral model for floating and fixed areas respectively. Clearly this model does represent an improvement, as the discrepancy between optical and UV areas has been reduced when they are allowed to float, and the quality of fit is substantially better if they are fixed to be the same. This does not appear to be the whole story, however, as a discrepancy remains. This is probably a consequence of the cooler response from the companion star (which is inferred to contribute; see Section 7.1). We tried adding another black body component, but found that beyond this point fits were poorly constrained and multiple solutions were possible, all yielding good fits with no discrepancy in optical and UV areas. We feel that a better way to approach this problem is to use a model of the binary following the approach of O’Brien et al. (2002), in which the binary geometry reduces the independence of the parameters that we currently have using arbitrary components. Such a model would, however, benefit from information gleaned from other aspects of our dataset, for example the orbital

lightcurves, so we defer this treatment to Paper III.

As a precursor to examining MB1 and MB3, for which only optical data are available, we also tested fitting optical and UV lightcurves separately. We initially tried fitting with all the parameters left free, but found that the problem was then very poorly constrained; a single bandpass did not allow us to uniquely determine both minimum and maximum temperatures. The formal minimum for an optical-only fit occurs for very low  $T_{\text{min}} \sim 3500$  K. While this may be of order the stellar temperature, the regions of the star exposed to bursts are also exposed to persistent radiation, and should not be this cool. Furthermore, this solution is strongly inconsistent with the UV lightcurve, and is only a shallow minimum;  $\chi^2$  is virtually constant for all  $0 < T_{\text{min}} < 50,000$  K. We thus chose to instead fix  $T_{\text{min}}$  to the value determined by the joint fit, 18,500 K. The parameters derived in this case (MB2-5 and MB2-6) were not significantly different from those based on the joint fit. The lags cannot be reliably compared, due to the uncertainty in *HST* timing, but there is no significant difference between the widths derived.

One important statement can be made from these analyses. Independently of whether we fit optical and UV data jointly or separately, and regardless of the spectral model assumed, we derive essentially the same lags and widths, i.e. the transfer function derived is robust and not sensitive to these assumptions. This means we can usefully compare transfer functions from different bursts that do not have UV coverage, and without knowing the correct spectral model to use.

### 5.3.3. The double burst (MB3)

We now consider the double burst, MB3. This is a more complex case than MB1 but occurred only about four hours (one binary orbit) after MB2 on the same night, so there are less likely to have been large changes in the accretion flow geometry than for the first burst which occurred about 20 hours (5 binary orbits) earlier. Since MB3a and MB3b are so close together, we perform a fit to both simultaneously, as this will provide a visual check of the consistency between the two bursts. The major difficulty with these bursts is that they exhibit

dips, most prominently around 35 s and 360 s. These dips are clearly not present in the optical data, and appear more prominent at low energies (Fig. 3). This suggests that the dips are due to absorption of the X-rays, and should be excluded from any attempt to model the optical data. We do this by masking out regions of the optical lightcurve that would be affected. The masked regions are indicated in Fig. 7.

As for MB2,  $T_{\min}$  is not meaningfully constrained by the data in the absence of UV coverage. For  $T_{\min} \gtrsim 6000$  K,  $\chi^2$  is virtually constant, and while cooler solutions are formally favored, we choose to ignore them for the reasons described above. A fit with  $T_{\min} = 18,500$  K is not visibly worse than one with very low  $T_{\min}$ , so we choose to use this value for lack of better information. This will facilitate a more direct comparison with MB2.

The fits to the lightcurves of both MB3a and MB3b are shown in Fig. 7, and parameters are given in Table 4. Given that only  $T_{\min}$  is externally constrained, the agreement with MB2 is striking.  $\tau_{\text{opt}}$  values agree within uncertainties and  $\sigma_{\tau}$  virtually agrees. A slightly larger width is derived from MB3, but the difference may not be significant. It would be expected if the response arises from a combination of disk and companion star, however, as MB3 occurred around phase 0.5 when the lag from the companion star is maximized. The difference in temperatures and areas is larger, but may be related to each other. We have artificially fixed  $T_{\min}$ , which will have the effect of also constraining  $T_{\max}$ . If  $T_{\min}$  had actually increased between bursts, then the corresponding  $T_{\text{irr}}$  would also have been higher, and a lower area would have been required to fit the MB3 fluxes. For example, a fit with  $T_{\min}$  fixed to 21,000 K greatly reduces the discrepancy between  $T_{\text{irr}}$  and  $A_{\text{opt}}$  between MB2 and MB3. Without UV data, however, we cannot say which of these (or other) combinations are correct, so have chosen to assume that  $T_{\min}$  does not change.

### 5.3.4. The first burst (MB1)

We have left MB1 until last as this is the least constrained case. We do not have UV data allowing independent fits of  $T_{\min}$  and  $T_{\max}$ , but neither are we well justified in assuming similarity to MB2 or MB3. MB1 occurred on the preceding night, and also at phase 0.2 when our visibility of the system was significantly different. We might then expect any of the parameters to be different. Nonetheless, we will begin from the same starting point as for MB3, i.e. assuming that  $T_{\min} = 18500$  K, as for MB2, and performing an unconstrained fit on the other parameters. This burst is more problematic than the preceding ones, as there are actually two plausible solutions differing mainly in the width of the transfer function. We show in Fig. 8 the dependence of normalized  $\chi^2$  on the Gaussian width,  $\sigma_{\tau}$  for all three bursts. For MB2 and MB3 there was a single, well-defined minimum, and the location is approximately the same for these two bursts. This width is clearly not consistent with the data from MB1, and a narrower transfer function is required. Formally the best fit occurs for a very narrow transfer function: MB1-1 as listed in Table 4.  $\chi^2$  is a rather complex function of  $\sigma_{\tau}$  in this region, and the best fit represents a very narrow minimum (hence the unrealistically small uncertainties for  $\sigma_{\tau}$  in model MB1-1). These characteristics suggest that the behavior at small

$\sigma_{\tau}$  may reflect random correlations in the noise between X-ray and optical lightcurves. A secondary minimum is present corresponding to a broader transfer function, model MB1-2. This minimum more closely resembles those seen for MB2 and MB3, and we suspect that this could be the true solution. In support of this, we show both models fitted to the data in Fig. 9. Model MB1-1 predicts a steeper optical rise than observed, whereas MB1-2 gives approximately the correct rise time. It is not obvious in what respect MB1-1 is preferred, also indicating that it could owe more to fitting the noise than to fitting the real structure. We will therefore adopt MB1-2 as the preferred fit to this burst.

The parameters obtained do seem plausible. We derive a shorter lag and narrower lag distribution (independently of whether we adopt MB1-1 or MB1-2). Both are to be expected at phase 0.2, as the companion star will make less contribution, and will do so at a shorter lag. The temperature and area derived are comparable, although a smaller reprocessing area is found, again as expected at this phase. Based on these parameters there is no need to invoke significant differences in the geometry or temperature of the reprocessing regions between the two nights.

Nonetheless we did attempt fits with a range of  $T_{\min}$  values. As for other bursts we find that formally the best fits are for unphysically low base temperatures ( $T_{\min} \lesssim 4000$  K), but that a large range of values larger than this also give acceptable fits. There is no reason to prefer a different  $T_{\min}$  value to MB2 or MB3.

## 6. THE ULTRAVIOLET BURST SPECTRUM

As our MB2 UV data were obtained in a spectroscopic mode, as well as obtaining the lightcurve of the reprocessed burst, we have a unique opportunity to examine its spectrum. Fig. 10 shows the spectrum of the extra light during the first 100 s of the burst. This was constructed by extracting a series of 100 s sub-spectra using the STSDAS task INTTAG and processing them in the same way as regular spectra. The non-burst spectrum was defined from 300 s intervals before and after the burst. More details of the spectral reduction will be provided in Paper II.

The burst spectrum appears to be continuum dominated with only a weak contribution from the lines. C III 1175 Å is particularly strongly enhanced, and to a lesser extent N V 1240 Å, but neither dominate the flux. The burst is not pronounced at all in C IV 1550 Å or He II 1640 Å.

The continuum shape is consistent with the burst models described earlier, being well fitted by the difference between a black body with temperature  $\sim 27,000$  K and one at  $\sim 18,500$  K. The upper temperature corresponds to the expected flux-weighted average temperature during the 100 s interval contributing to the burst as calculated from model 1 for MB2. This shows that the model does reproduce the wavelength dependence as well as the temporal evolution. It also indirectly supports our low reddening value ( $E(B-V) = 0.06 \pm 0.03$ ) derived from the 2175 Å interstellar feature (Paper III). If this reddening had been underestimated due to an anomalously weak 2175 Å feature then in general we would not expect the temperature implied by the shape of the spectrum to be consistent with that earlier obtained only

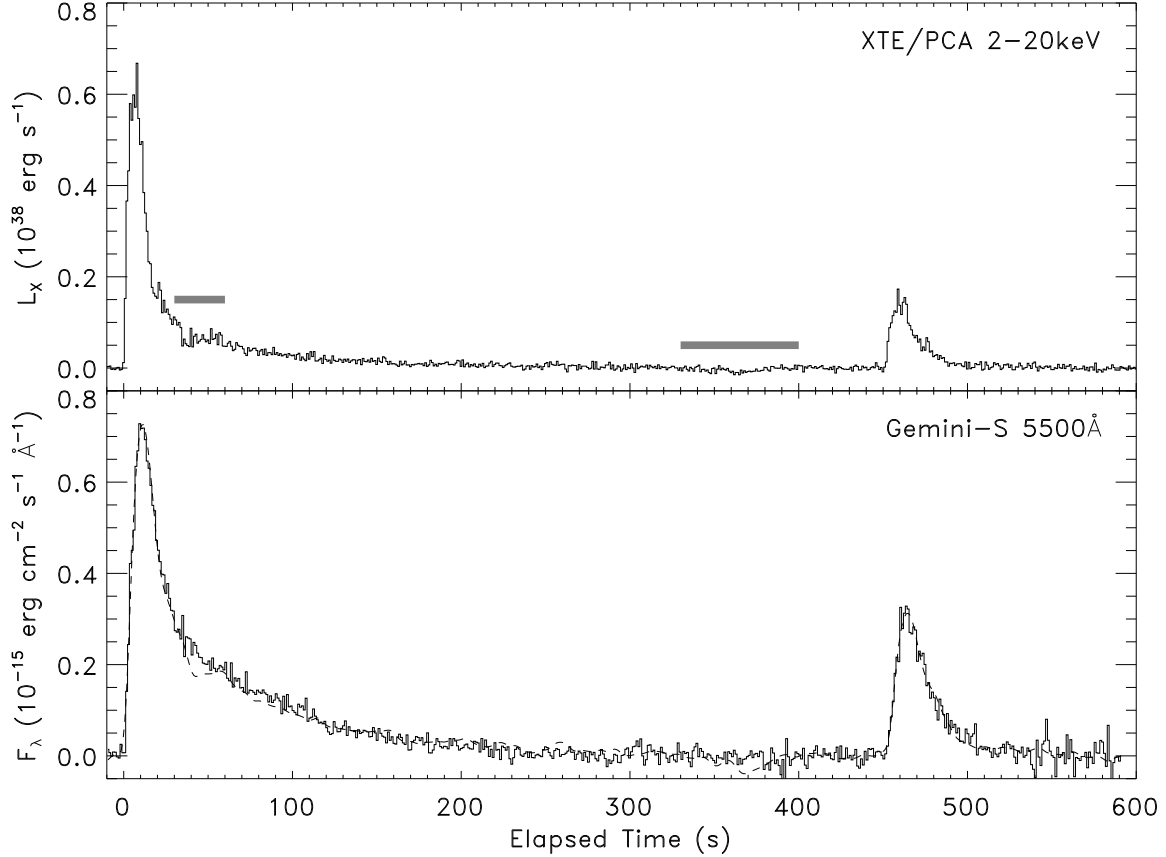


FIG. 7.— Single black body joint-fit to both MB3a and MB3b. The underlying non-burst X-ray luminosity that has been subtracted off is  $1.9 \times 10^{36} \text{ erg s}^{-1}$ . Gray bars indicate X-ray dipping regions. These were retained in calculating the model optical lightcurve but were masked out of  $\chi^2$  calculation. The discrepancy between the model and the optical data at these points is further evidence that the dips are a consequence of our changing visibility of the X-ray source, not a true change in the unabsorbed luminosity.

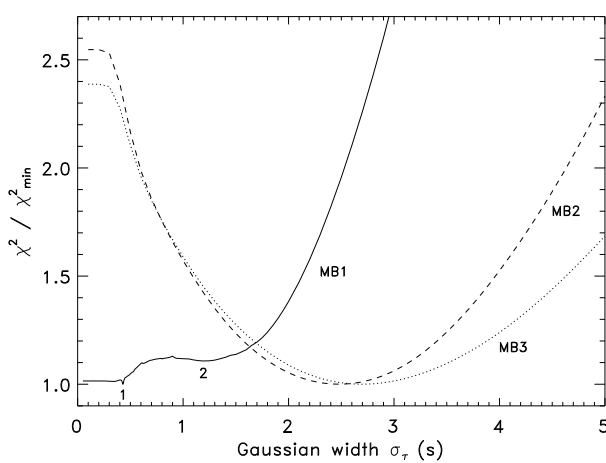


FIG. 8.— Normalized  $\chi^2$  as a function of Gaussian width for each burst. For each point the width was fixed, but other parameters were optimized to find the best fit. Annotations 1 and 2 for MB1 refer to the two minima given as solutions in Table 4. Note that all curves flatten below  $\sigma_\tau \sim 0.3 \text{ s}$ , corresponding to a Gaussian FWHM less than 0.7 s, and less than the optical time-resolution.

from time-dependence of the reprocessed light, and the

far-UV spectrum would be redder.

## 7. DISCUSSION

### 7.1. Evidence for phase dependence of the burst response

One of the primary goals of echo mapping is echo tomography: phase-dependent echo maps in which different components, such as the disk and companion star, can be disentangled based on different amplitudes and phasings of phase dependence. In principle this technique could even be used to obtain a direct measure of the binary separation and orbital inclination independent of other constraints. Real datasets have, however, fallen far short of these aspirations, and we certainly would not claim that the results presented here fulfill the hopes of echo-mapping. Nonetheless, we do see changes in the response, and it is worthwhile to investigate if they are consistent with expected phase-dependent changes, and can constrain the parameters of UY Vol.

One of the major limitations, of course, is that MB1 was obtained on a different night to MB2 and MB3. Since MB1 provides the main sensitivity to phase-dependent changes, we must apply the caveat that the differences observed could reflect secular changes in the actual reprocessing geometry rather than just differences in our viewing angle. The persistent (pre-burst) X-ray flux is essen-

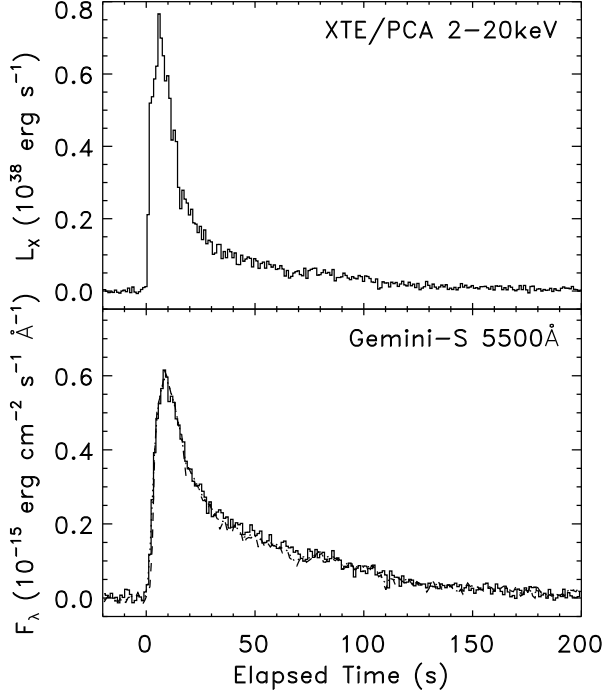


FIG. 9.— Single black body fits to MB1. The underlying non-burst X-ray luminosity that has been subtracted off is  $1.6 \times 10^{36} \text{ erg s}^{-1}$ . The dotted line corresponds to the formal best fit, MB1-1 in Table 4. The dashed line corresponds to the broad secondary maximum which we suspect may be the true solution, MB1-2. Note that the latter fits the rise time of the optical burst better.

tially the same for MB1 and MB2. It is lower for MB3, but there is some evidence for dipping at this time. This implies no substantial difference in the accretion rate between the MB1 and MB2 epochs. Optical lightcurves will be compared in Paper III and should be very sensitive to changes in the reprocessing geometry between epochs. The optical lightcurve at the time of MB1 is somewhat different, but the differences are not dramatic and may primarily reflect different realizations of the strong flickering which is present in the optical data. The amplitude of the differences between MB1 and MB2 epochs ( $\lesssim 25\%$ ) is comparable to that between MB2 and MB3 epochs, and also to the amplitude of individual flickering events. There is thus no compelling evidence for a change in the state of the system, but this possibility cannot be securely discounted.

Assuming it is reasonable to compare the responses from the three bursts, the major difference is that MB2 and MB3 both have responses that are lagged and smeared by more. This is as expected from their phases. Fig. 11 shows predicted responses as a function of orbital phase calculated using the methods described by O’Brien et al. (2002) for model 2 ( $q = 0.2$ ). Given the limitations inherent in approximating the true response with a Gaussian, the range of lags observed is in reasonable agreement with predictions. In particular, we do expect that MB2 (phase 0.38) will have a similar lag distribution to MB3 (phase  $\sim 0.5$ ), whereas we expect a quicker and less smeared response from MB1, as

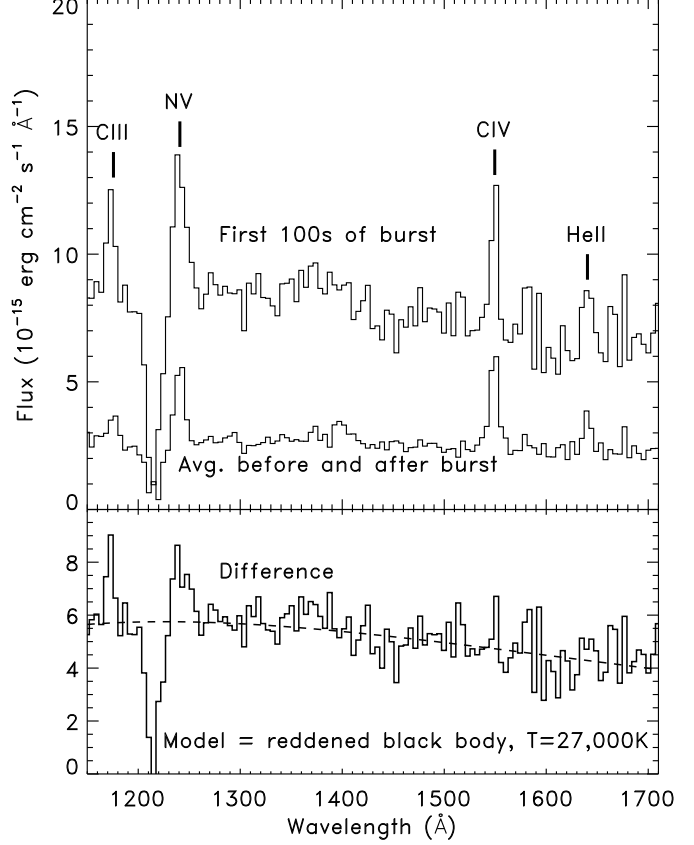


FIG. 10.— Far-UV spectrum of MB2. The upper panel shows the spectrum of the first 100 s of the burst compared to that before and after. The lower panel shows the difference between the two. The dashed line shown in the lower panel is the expected black body burst spectrum based on the time-averaged temperature evolution fitted earlier. All spectra shown here have been rebinned to  $4.7 \text{ \AA}$  per pixel.

observed. The amplitude of the difference between responses is in approximate agreement with expectations. When plotted in this way, it is apparent that all bursts appear to show the onset of a strong response at approximately the same time, but that MB2 and MB3 extend for longer beyond that.

While the general picture is in agreement with predictions, it is clear that the data are not precise enough to constrain the system parameters further. Nonetheless, the very fact that the response appears to change with phase, and with such a large amplitude, does indicate significant response from the companion, and the large smearing of the response around phase 0.5 indicates that the disk must also contribute.

We can also consider these results in the context of other observations of this and other sources. The comparison of most interest is with Schoembs & Zoeschinger (1990). These authors found that optical bursts (with no simultaneous X-ray coverage) exhibited longer rise times when the companion star would be on the far side of the disk. This is equivalent to saying that the smearing increases close to phase 0.5 (as we also find), provided that the intrinsic rise time of the X-ray bursts is the same. The large dispersion in the response that we see close to

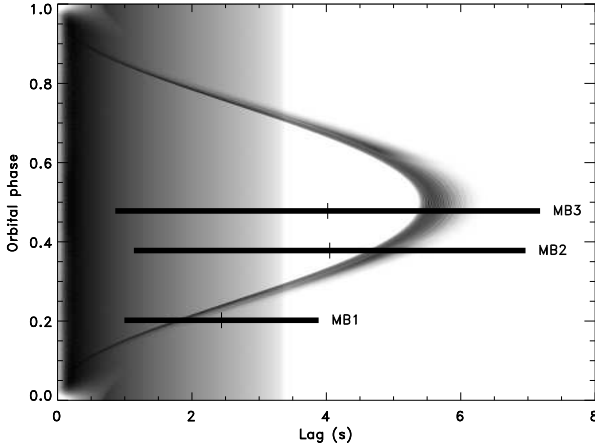


FIG. 11.— Predicted echo tomogram calculated according to O’Brien et al. (2002). The broad non-varying region to the left is the disk, the moving component is the irradiated face of the companion star. Solid bars indicate the response inferred from Gaussian fitting of MB1 (lower), MB2 (middle), and MB3a and b combined (upper). The bar represents the lags over which the Gaussian model is above half response (i.e. its length is the full-width at half maximum).

phase 0.5 is also not unprecedented. Similar dispersions were found by Truemper et al. (1985) for 4U 1636–536, and by Kong et al. (2000) for GS 1826–24. In all of these cases they likely indicate contribution from both disk and companion, as a response from the companion alone will vary in lag, but should always have a relatively narrow response.

## 7.2. Local diffusion time delays

There are two likely sources of smearing of the reprocessed signal. The delays most commonly discussed (and considered so far) are those from light-travel times across the binary; global delays. A finite reprocessing time could also introduce a local delay. X-rays above about 1 keV will experience a low-enough photo-electric absorption opacity to deposit energy at a significant optical depth in an atmosphere. Reprocessed energy will then have to diffuse outward, and so there will be an additional diffusion time delay.

This topic was considered initially by Pedersen et al. (1982) in analyzing bursts from 4U 1636–536. They estimated that the diffusion time for a typical photon would be  $\sim 0.6$  s, largely negligible compared to the expected light travel time delays. Cominsky, London, & Klein (1987) examined the problem more rigorously, calculating time-dependent responses of a hot stellar atmosphere to an X-ray burst, including the effect of the burst on the atmospheric temperature structure and opacities. Their results were in agreement with those of Pedersen et al. (1982), and they found that 50 % of the reprocessed light is expected within just 0.2 s, but that there was also a very extended tail to the response up to 10 s. Finally, McGowan et al. (2003) also considered this issue, but neglected photo-absorption, which will be critical for the soft X-rays produced in a burst. Based on these calculations, we would not expect our method to be significantly affected by reprocessing times, as a Gaussian

response approximation will be dominated by when most of the light emerges, and this occurs within a fraction of a second. Indeed, our observations are broadly consistent with expectations from light travel time delays and, allowing for the limitations of the Gaussian approximation, do not obviously require additional local delays.

This conclusion may be different from that obtained for correlated flickering in the low-mass X-ray binaries Sco X-1 and LMC X-2, for which McGowan et al. (2003) argue that lags may be too long for light travel times alone. More and better data are needed to confirm this discrepancy, but if confirmed the key difference may be in the nature and spectrum of the X-ray irradiation. Cominsky, London, & Klein (1987) also considered harder irradiation than that provided by an X-ray burst, and found that it could increase the diffusion timescale significantly (see also McGowan et al. (2003)). Thus while reprocessing times are of marginal significance in considering burst reprocessing, they may be of more importance for other applications where further investigation is needed. The corollary of this is that the relatively soft irradiation of bursts may provide the least biased way to isolate light travel time delays and hence the ideal signal for echo-tomography.

## 7.3. Expected temperatures

It is interesting to compare the deduced reprocessing temperatures with those expected based on the X-ray luminosity, as this provides a test of the reprocessing efficiency. We will consider MB2, for which the temperatures are best constrained. For this burst, the persistent luminosity (at 6.8 kpc) was  $2.1 \times 10^{36}$  erg s $^{-1}$  and the peak burst luminosity was  $6.9 \times 10^{37}$  erg s $^{-1}$ .

Irradiation of the companion star is sensitive to the mass ratio, as smaller companions will more readily be shielded by the disk. For example, if we take model 1 ( $q = 0.08$ ) and the typical effective disk opening angle of 12° deduced by de Jong, van Paradijs, & Augusteijn (1996) then the companion would be completely shielded. This is clearly not the case, as the companion can directly eclipse the neutron star, but we cannot quantify how directly it is illuminated. Note that the opening angle need not be that of the disk rim, but could represent material in the inner disk that can shield the companion. For models 2 and 3, calculations are more straightforward and the differences between the two are less dramatic. For a disk opening angle of 6° we expect angles of incidence of greater than 45° from normal, increasing to 60° for opening angles of 12°. We assume an X-ray albedo for the companion of  $\sim 0.4$  following de Jong, van Paradijs, & Augusteijn (1996). We then expect the highest persistent irradiation temperature on the companion of 16,000–21,000 K depending on mass ratio (for the range 0.20–0.34) and disk opening angle (in the range 6–12°). This is the temperature at the point closest to the compact object and most of the irradiated region is at temperatures less than this as the angle of incidence is steeper. At the burst peak we would expect temperatures of 38,000–50,000 K.

For the disk we estimate the estimated temperature at the disk rim using the semi-empirical prescription of Dubus et al. (1999) and Dubus et al. (2001). Assuming Dubus’ estimate of the irradiation efficiency and a disk radius of  $5 \times 10^{10}$  cm we expect a persistent irradiation

temperature of 9000 K and a peak burst temperature of 21,000 K. Both of these are the lowest temperatures in the disk, and most of the disk area is hotter than this (the opposite case to that calculated for the companion star). For comparison, the persistent luminosity of  $2.1 \times 10^{36}$  erg s $^{-1}$  corresponds to a mass transfer rate of  $\sim 1.2 \times 10^{16}$  g s $^{-1}$ . For a steady state lobe-filling disk the effective temperature due to viscous heating should be just 2500 K, indicating that the disk is in a regime that can only remain in a high state with irradiative heating.

Our earlier conclusions that the reprocessed bursts likely arise from a combination of emission from the companion star and disk are consistent with these calculations. Our estimate of the peak reprocessing temperature is 35,000 K. The irradiated area of the companion star is expected to have temperatures possibly extending up to 50,000 K, while the disk could plausibly have temperatures from 21,000 K upward. The temperature ranges are overlapping, with the greater distance to the companion offset by its more direct illumination, and are consistent with our observations.

## 8. CONCLUSIONS

We have reported several simultaneous X-ray bursts in the low-mass X-ray binary UY Vol, including the highest quality reprocessed optical coverage, and the only reprocessed UV burst that we are aware of in any source. These results allow a more thorough test of the paradigm for reprocessing of X-ray bursts, and reprocessing of X-ray emission in general, than previously possible. Several key assertions about reprocessing have been tested.

i) X-rays are absorbed at relatively high optical depths, thermalized, and re-emitted with a quasi-black body spectrum. By obtaining the UV spectrum of the extra light produced during a burst, we have shown that it is indeed dominated by continuum emission, and that the shape of that continuum is consistent with black body emission with temperatures as inferred from the lightcurves of the bursts. The discrepancy with the optical flux, however, suggests that a single-temperature black body model is not sufficient.

ii) Reprocessed emission in the optical and UV is lagged predominantly by light travel times rather than by local photon diffusion. This appears to be borne out by our observations as light travel times are sufficient to

explain the lags and smearing observed. Note that this conclusion (and the preceding one) may not be true in general, but may be specific to irradiation with the spectrum of an X-ray burst. Harder or softer irradiation is likely to produce a different response.

iii) X-rays are reprocessed both by the accretion disk and by the companion star. This is supported by our observations, as we do appear to see a phase-dependence of both the lag and the smearing of the response. If the response came from the disk alone, we would expect little variation. If it came from the companion alone, we predict variations in the lag, but not in the smearing. The temperatures that both the disk and companion are expected to reach during a burst are consistent with our observations. The failure of a single-zone reprocessor model to explain the relative UV and optical fluxes in the burst also supports a multi-component response. Our observations do not appear to resolve distinct lags from disk and companion, however, possibly a consequence of the long bursts exhibited by UY Vol. Sources which exhibit short duration bursts may be better suited to this analysis.

This work includes observations with the NASA/ESA *Hubble Space Telescope*, obtained at STScI, which is operated by AURA Inc. under NASA contract No. NAS5-26555. Support for *HST* proposal GO 9398 was provided by NASA through a grant from STScI. RIH also acknowledges support by NASA through Hubble Fellowship grant #HF-01150.01-A awarded by STScI. This work uses observations obtained at the Gemini Observatory, which is operated by the AURA Inc., under a cooperative agreement with the NSF on behalf of the Gemini partnership: the National Science Foundation (United States), the Particle Physics and Astronomy Research Council (United Kingdom), the National Research Council (Canada), CONICYT (Chile), the Australian Research Council (Australia), CNPq (Brazil) and CONICET (Argentina). We would like to thank Rodrigo Carrasco and the other staff involved in obtaining these data for putting in the extra effort to make this unusual observation a success! RIH would like to thank Danny Steeghs for obtaining prior imaging of the field to aid our *HST* preparation. This work has made use of the NASA Astrophysics Data System Abstract Service.

## REFERENCES

Chabrier, G., & Baraffe, I. 2000, ARA&A, 38, 337  
 Cominsky, L. R., London, R. A., & Klein, R. I. 1987, ApJ, 315, 162  
 de Jong, J. A., van Paradijs, J., & Augusteijn, T. 1996, A&A, 314, 484  
 Dubus, G., Lasota, J.-P., Hameury, J.-M., & Charles, P. 1999, MNRAS, 303, 139  
 Dubus, G., Hameury, J.-M., & Lasota, J.-P. 2001, A&A, 373, 251  
 Fitzpatrick, E. L. 1999, PASP, 111, 63  
 Fukugita, M., Shimasaku, K., & Ichikawa, T. 1995, PASP, 107, 945  
 Gaskell, C. M., Peterson, B. M. 1987, ApJS, 65, 1  
 Gottwald, M., Haberl, F., Parmar, A. N., & White, N. E. 1986, ApJ, 308, 213  
 Haswell, C. A., Hynes, R. I., King, A. R., & Schenker, K. 2002, MNRAS, 332, 928  
 Horne, K. 1994, Astronomical Society of the Pacific Conference Series, 69, 23  
 Horne, K., Welsh, W. F., & Peterson, B. M. 1991, ApJ, 367, L5  
 Hynes, R. I., O'Brien, K., Horne, K., Chen, W., & Haswell, C. A. 1998, MNRAS, 299, L37  
 Hynes, R. I., Haswell, C. A., Chaty, S., Shrader, C. R., & Cui, W. 2002, MNRAS, 331, 169  
 Hynes, R. I., Haswell, C. A., Cui, W., Shrader, C. R., O'Brien, K., Chaty, S., Skillman, D. R., Patterson, J., Horne, K. 2003, MNRAS, 345, 292  
 Hynes, R. I., in "The Astrophysics of Cataclysmic Variables and Related Objects", ASP Conf. Ser. Vol. 330, Eds. J. M. Hameury & J. P. Lasota, p237  
 Jahoda, K., Markwardt, C. B., Radeva, Y., Rots, A. H., Stark, M. J., Swank, J. H., Strohmayer, T. E., Zhang, W., 2006, ApJS, in press  
 Jonker, P. G., & Nelemans, G. 2004, MNRAS, 354, 355  
 Jonker, P. G., Steeghs, D., Nelemans, G., & van der Klis, M. 2005, MNRAS, 356, 621  
 Koen, C. 2003, MNRAS, 344, 798  
 Kong, A. K. H., Homer, L., Kuulkers, E., Charles, P. A., & Smale, A. P. 2000, MNRAS, 311, 405  
 Kuulkers, E., den Hartog, P. R., in't Zand, J. J. M., Verbunt, F. W. M., Harris, W. E., & Cocchi, M. 2003, A&A, 399, 663  
 Landolt, A. U. 1992, AJ, 104, 340

Lawrence, A., et al. 1983, *ApJ*, 271, 793

Liu, Q. Z., van Paradijs, J., & van den Heuvel, E. P. J. 2001, *A&A*, 368, 1021

McGowan, K. E., Charles, P. A., O'Donoghue, D., & Smale, A. P. 2003, *MNRAS*, 345, 1039

Naylor, T. 1998, *MNRAS*, 296, 339

O'Brien, K., Horne, K., Hynes, R. I., Chen, W., Haswell, C. A., & Still, M. D. 2002, *MNRAS*, 334, 426

Parmar, A. N., White, N. E., Giommi, P., Haberl, F., Pedersen, H., & Mayor, M. 1985, *IAU Circ.*, 4039

Parmar, A. N., White, N. E., Giommi, P., & Gottwald, M. 1986, *ApJ*, 308, 199

Pearson, K. J., et al. 2006, *ApJ*, submitted (Paper II)

Pedersen, H., et al. 1982, *ApJ*, 263, 325

Press, W. H., Teukolsky, S. A., Vetterling, W. T. & Flannery, B. P. 1992, *Numerical Recipes in C: The Art of Scientific Computing*, 2nd Edn., CUP, 1992, p408

Profitt, C., et al. 2002, *STIS Instrument Handbook*, Version 6.0, STScI, Baltimore

Schenker, K., & King, A. R. 2002, *ASP Conf. Ser.* 261: *The Physics of Cataclysmic Variables and Related Objects*, 261, 242

Schoembs, R. & Zoeschinger, G. 1990, *A&A*, 227, 105

Shahbaz, T., Casares, J., Watson, C. A., Charles, P. A., Hynes, R. I., Shih, S. C., & Steeghs, D. 2004, *ApJ*, 616, L123

Thorsett, S. E., & Chakrabarty, D. 1999, *ApJ*, 512, 288

Truemper, J., Sztajno, M., Pietsch, W., van Paradijs, J., & Lewin, W. H. G. 1985, *Space Science Reviews*, 40, 255

van Paradijs, J., van der Klis, M., & Pedersen, H. 1988, *A&AS*, 76, 185

Wade, R. A., Quintana, H., Horne, K., & Marsh, T. R. 1985, *PASP*, 97, 1092

White, R. J., Peterson, B. M. 1994, *PASP*, 106, 879

Wolff, M. T., Hertz, P., Wood, K. S., Ray, P. S., & Bandyopadhyay, R. M. 2002, *ApJ*, 575, 384

Wolff, M. T., Becker, P. A., Ray, P. S., & Wood, K. S. 2005, *ApJ*, 632, 1099